Materials Today Nano 25 (2024) 100462

Contents lists available at ScienceDirect

Materials Today Nano

journal homepage: www.sciencedirect.com/journal/materials-today-nano

Thermally stimulated structural evolution of bimetallic nanoplatelets - Changing from core-shell to alloyed to Janus nanoplatelets

Xiaobin Xie *, Alfons van Blaaderen **, Marijn A. van Huis ***

Soft Condensed Matter, Debye Institute for Nanomaterials Science, Utrecht University, Princetonplein 5, 3584 CC, Utrecht, the Netherlands

ARTICLE INFO

Keywords:
Noble metals nanoplatelets
Atomic diffusion
Core-shell
Alloy
Janus

ABSTRACT

Gold-based bimetallic nanostructures exhibit unique optical and catalytic properties that are strongly dependent on their composition and nanoscale geometry. Here we show the nano-structural transformation of mesoporous-silica-coated Au-M (Ag, Pd, Pt) core-shell nanoplatelets (NPLs) with a triangular shape to alloyed platelets at temperatures at least 300 °C below the lowest melting point of the metals while still retaining the out-of-equilibrium triangular shape and intact mesoporous shell. Before the alloying started the rough core-shell morphology of the Au–Pd and Au–Pt NPL systems were first observed to relax into a much smoother core-shell morphology. The alloying temperature was found to be related to the melting points and atom fractions of the shell metals; the higher the melting point and atomic fraction of the shell metal, the higher the temperature required for alloying. The highest alloying temperature was found for the Au–Pt system (650 °C), which is still hundreds of degrees below the bulk melting points. Surprisingly, a phase separation of Au and Pt, and of Au and Pd, was observed at 1100 °C while both systems still had an anisotropic plate-like shape, which resulted in Janus-like morphologies where the pure Pt and pure Pd ended up on the tips of the NPLs as revealed via in-situ heating in the scanning transmission electron microscope (STEM). The Janus-type morphologies obtained at elevated temperatures for the NPLs composed of combinations of Au–Pt and Au–Pd, and the smooth core-shell morphologies before alloying, are very interesting for investigating how differences in the bi-metallic morphology affect plasmonic, catalytic and other properties.

1. Introduction

Bi-metallic nanoparticles (BMNPs) have attracted great interest due to their promising applications in various fields, including catalysis [1–5] energy conversion [6–8], biological medicine [5,9,10], and sensing [11–13]. The combination of two different metals can improve their performance, realize bifunctional applications, and even leads to the development of new fields of research. For instance, by combining plasmonic metals such as Au or Ag with catalytic metals such as Pd or Pt, newly photocatalytic nanoparticles have been made for plasmonic enhanced photocatalytic reactions, including hydrogen evolution [14], oxidation [15], and reduction reactions [2,16]. In particular nanoparticles (NPs) based on Au nanoplatelets (Au NPLs) are increasingly drawing attention from the scientific community, because of their special morphology enabling highly tunable optical properties [17–19]. The localized surface plasmon resonances (LSPRs) of Au NPLs based BMNPs depend on their size, composition, and structure [5,20,21]. Furthermore, manipulating the spatial distribution of a second metal on Au NPLs allows adjusting the atomic and electronic structures of the nanocrystals, and thus, allows fine-tuning of the plasmonic and catalytic properties of these BMNPs for instance for enhanced photocatalysis and Raman scattering [5,22–24].

In the past few decades, a wide variety of BMNP structures, like core-shell, alloyed, Janus, yolk-shell and other complex morphologies have been successfully prepared via a great diversity of synthesis routes and techniques [5,25–27]. Among these NPs, the core-shell NPs are the most commonly prepared type, while alloyed and Janus NPs with well-defined shape usually display more unique properties, but are not easy to acquire by direct synthesis. Thermal treatment is one of the most popular ways for restructuring the morphology of metal-based microstructures and nanostructures [28]. In the case of colloidal nanoparticles, a necessary step is the removal of the ligands or surfactants

* Corresponding author.
** Corresponding author.
*** Corresponding author.
E-mail addresses: xb.xie@hotmail.com (X. Xie), a.vanblaaderen@uu.nl (A. van Blaaderen), m.a.vanhuis@uu.nl (M.A. van Huis).

https://doi.org/10.1016/j.mtnano.2024.100462
Received 28 November 2023; Received in revised form 4 February 2024; Accepted 19 February 2024
Available online 20 February 2024

covering the surface of the NPs before these can be used for catalysis [8,29]. Another approach is to use a mesoporous coating onto the metal NPs [30]. Such silica layers are not only useful in reducing the large van der Waals forces, but also can be used to stabilize out-of-equilibrium NP shapes such as rods against deformation back into an equilibrium shape [31–33]. Recently, in-situ heating transmission electron microscopy (TEM) has emerged as a powerful technique for investigating the dynamic processes associated with morphological evolutions, structural transitions, and phase behavior at nano and atomic length scales caused by heating [34–39]. In particular, the imaging provides real-space probing of processes that are often out-of-equilibrium and provide therefore important insights into both thermodynamic driving forces and kinetic factors affecting shape changes at the nanoscale. Previous work has shown the importance of performing such experiments not only in-situ in an electron microscope, but also ex-situ e.g. in an oven as even an almost invisible deposited layer of carbon on noble metal NPs can strongly affect how they respond to heating [33]. In both in-situ and ex-situ conditions, the formation of fully alloyed Au-M (Ag, Pd, and Pt) nanorods (NRs), Au–Ag nanospheres, and NPLs, Au–Pd and Au–Pt nanospheres has been achieved experimentally by heating their corresponding Au-M (Ag, Pd, and Pt) core-shell particles to the proper temperatures [32,40–44]. Moreover, simulation studies have been performed to gain understanding of the melting, alloying, and phase behavior of (bi-)metallic nanoparticles [40,45–48]. Phase segregation of Au-M (Pd, Pt) nanoparticles was predicted in the small size regime (up to ~20 nm) for spheres and truncated octahedrons [49–52]. We mention here that the vast parameter space was recently also explored computationally by Eom et al. [53], wherein the authors compared the energetics of various core-shell, mixed, and Janus-like bimetallic nanosystems. However, the experimental realization of alloying and phase segregations of Au-M (Ag, Pd, Pt) having well-defined platelet shapes has not been mostly explored yet as far as we know, with the exception of the work described in Ref. [40] in which the alloying of Au–Ag nanotriangles (NTs) was investigated and compared with Au–Ag nanorods experimentally and by molecular dynamics computer simulations.

In this work, we systematically investigated the alloying and phase segregation of Au NT core and Ag, Pd, Pt shell bimetallic NPLs with a triangular shape under the confinement by a ~20 nm $mSiO_2$ outer shell, via a combination of in-situ TEM heating and ex-situ oven heating. By heating the Au-M (Ag, Pd, Pt) core-shell NPLs to a proper temperature, Au–Ag, Au–Pd, and Au–Pt bimetallic alloyed NPLs with a well-defined far out-of-equilibrium triangular shape were obtained. The alloying processes were monitored by in-situ STEM imaging at each heating temperature and corroborated by ex-situ oven heating experiments. The alloyed NTs were further heated to a final temperature of 1100 °C to investigate the phase behavior. The Ag–Au NPLs become more rounded in shaped, but remained alloyed and remained strongly anisotropic plate-like shaped even at these high temperatures. Unexpectedly, phase-separation was found to take place both for Au–Pd and Au–Pt systems at 1100 °C, while again the shape remained plate-like resulting in Janus-like Au–Pd and Au–Pt NTs. The well-retained triangular shape even at such high temperatures, is due to the confining effect of the $mSiO_2$ outer shell and allows for the creation of new morphologies of both alloyed and Janus-type particles next to the original core-shell particles that will be important model systems for investigating the role of morphology on anisotropic bimetallic nanoparticles.

2. Materials and methods

2.1. Materials

Used chemicals were: Hydrogen tetrachloroaurate (III) hydrate ($HAuCl_4$, 99.9%, Sigma), Sodium borohydride ($NaBH_4$, 96%, Sigma), Silver nitrate ($AgNO_3$, ≥99.9%, Sigma), Sodium tetrachchloropalladium (II) (Na_2PdCl_4, 99.95%, Sigma), Potassium tetrachchloroplainate (II) (K_2PtCl_4, 99.95%, Sigma), L-ascorbic acid (AA, 99.98%, Sigma), Salicylic acid (SA, 99.9%, Sigma), Sodium hydroxide (NaOH, 98%, Sigma), Tetraethyl orthosilicate (TEOS, $Si(OC_2H_5)_4$, 99.0%, Sigma-Aldrich), Methanol (MeOH, 99%, Sigma), and Cetyltrimethyl-ammonium chloride (CTAC, ≥99%, Sigma), and CTAC solution (25 wt% in water, Sigma-Aldrich). All chemicals were used as received without further purification. Also, de-ionized water with a resistivity of 18.2 MΩ•cm at 25 °C was used in the experiments.

2.2. Synthesis and purification of Au NTs

The Au NTs were synthesized by a modification of a previously reported synthesis [54]. (1) Au seeds@CTAC: 25 μL of 50 mM $HAuCl_4$ were mixed with 4.70 mL of 0.10 M CTAC solution in a 20 mL glass vial. Next, 300 μL of freshly prepared 10 mM $NaBH_4$ was injected into the above mixture while strongly stirring for 2 min. After that, it was kept at room temperature for at least 2 h. After 2 h, the Au seeds solution was diluted 10 times by mixing 0.50 mL of Au seeds and 4.50 mL of 0.10 M CTAC. (2) 1.60 mL of 0.10 M CTAC, 40 μL of 50 mM $HAuCl_4$, and 30 μL of 10 mM KI were added into 8.00 mL of de-ionized water in a 20 mL glass vial one by one. This solution was marked as solution-A. (3) 60 mL of deionized water was added into a 250 mL round-bottom flask. 60 mL of 0.10 M CTAC, 1.5 mL of 50 mM $HAuCl_4$, and 900 μL of 10 mM KI were injected into the deionized water. This solution was marked as solution-B. (4) 40 μL and 1.20 mL of 0.10 M AA solution were injected into solution-A and solution-B, respectively, while stirring. After both the solution-A and solution-B turned colorless in 30 s, 100 μL of diluted Au seeds was injected into solution-A. Stirring continued for about 1 min. All solution-A was added into solution-B while stirring. After the two solutions were well mixed, it was left undisturbed for about 2 h, which allowed growth of the Au nanocrystals. (5) Purification: After allowing growth for about 2 h, 34 mL of solution-B and 4.50 mL of 25 wt % CTAC were mixed in a 50 mL centrifuge tube, and then left undisturbed for 12 h. The suspension was removed carefully, and the sediment was suspended in 35.0 mL of 0.010 M CATC and served as a stock solution for further use.

2.3. Synthesis of Au NT-M (Ag, Pd, & Pt) core-shell nanoparticles

The Au NT-Ag core-shell nanoparticles (NPs) were synthesized by modifying our previous reported protocol [55]. In brief: a volume of 7.7 mL of Au NTs stock solution (λ_{LSPR} = 657 nm, maximum extinction = 2.1) was mixed with 2.1 mL of deionized water in a 20 mL glass vial. 150 μL of 0.010 M $AgNO_3$ and 100 μL of 0.10 M AA were added into the above Au NTs solution under stirring. The solution was stirred at room temperature (RT) for 12 h.

The Au NT-Pd core-shell NPs were prepared using a previous reported method [55] with modification. In brief, a volume of 7.7 mL of Au NTs stock solution (λ_{LSPR} = 657 nm, maximum extinction = 2.1) was mixed with 2.1 mL of deionized water in a 20 mL glass vial. 150 μL of 0.10 M Na_2PdCl_4 and 100 μL of 0.010 M AA were added into the above Au NTs solution under stirring. The solution was stirred at RT for 12 h.

The Au NT-Pt core-shell NPs were prepared via modifying a previous reported protocol [55]. In brief: a volume of 7.7 mL of Au NTs stock solution (λ_{LSPR} = 657 nm, maximum extinction = 2.1) was mixed with 2.1 mL of deionized water in a 20 mL glass vial. 150 μL of 0.010 M K_2PtCl_4 and 100 μL of 0.10 M AA were added into the above Au NTs solution under stirring. The solution was stirred at 60 °C for 12 h.

2.4. Synthesis of Au NT-M-$mSiO_2$ core-shell-shell nanoparticles

The Au NT-*M*-$mSiO_2$ core-shell-shell (CSS) nanoparticles (NPs) were synthesized using a modified protocol from previously report [56]. In brief: a volume of 10 mL of as-prepared Au NT-M solution was centrifuged at 10000 rcf (relative centrifugal force) for 10 min (Rotina 380R Hettich centrifuge). After centrifuging, the supernatant was removed,

and the sediment was suspended in 10 mL of deionized water and transferred into a 20 mL glass vial. 100 μL of 0.10 M CATC and 100 μL of 0.10 M NaOH were added into the above Au NT-M solution. Finally, 100 μL of 20 vol% TEOS in methanol was injected into the above solution in one shot under stirring. After 15 min, again, another 100 μL of 20 vol% TEOS in methanol was injected into the above solution in one shot under stirring. The solution was stirred for 45–48 h. The Au-*M*-mSiO_2 core-shell-shell NPs were collected by centrifuged 10 mL of the above solution at 10000 rcf for 10 min (Rotina 380R Hettich centrifuge) when the reaction was done. The as-synthesized NPs were washed by 2.0 mL of de-ionized water and 2.0 mL of ethanol, respectively, and finally suspended in 2.0 mL of ethanol.

2.5. Heating experiments

In-situ heating: In-situ heating (S)TEM experiments were performed using a heating holder (DENS-H-SH30-FS01) made by DENS Solutions. Heating chips (Wildfire S3 Nano-Chip GT, P.T.H.SS.1, Wnr: DS2313-W2) with electron beam transparent SiN_x windows were provided by the same company. (1) The heating chips were pretreated using an Ar/O_2 (20 vol% of O_2) plasma treatment for 20 s at RT. (2) 8.0 μL of the as-prepared Au NT-*M*-mSiO_2 NPs were dropped on a heating chip and dried in ambient air at RT. (3) The heating chip with the sample was mounted on a heating holder (DENS-H-SH30-FS01). (4) The heating holder was inserted into the Electron Microscope used, which was a FEI Talos F200X. (5) Normally, the heating procedure started from 20 °C to an aimed final temperature with steps in temperature of 50 °C or 100 °C, at least 5 min waiting at each temperature before acquiring (S)TEM images, the heating protocols are shown in the main text. The heating curve for each sample is presented in their corresponding figure.

Recording (S)TEM images and videos: The experiments were performed on a FEI Talos F200X, operating at 200 kV. The STEM images were acquired by using a camera length of 98 mm to reduce diffraction electron effects and high angle annular dark field detector with the TEM Image Analysis (TIA) software. The videos were recorded by TIA software (Version 5.0) using the preview mode and a recording speed of 1 fps. The final videos shown in Supporting Information were processed by ImageJ software (Version 1.51j8) and are displayed 15 times faster than real-time.

2.6. Characterization

Ultraviolet–Visible (UV–Vis) spectroscopy was performed with a Lambda 750 UV–Vis spectrograph (PerkinElmer). Transmission electron microscopy (TEM) images and scanning transmission electron microscopy high angle annular dark-field (STEM-HAADF) images were acquired with a FEI Talos F200X, operated at 200 kV and equipped with a ChemiSTEM EDX detector that was used for the EDS maps displayed in all the relevant Figures.

3. Results and discussion

3.1. Morphology, structure, and optical property of as synthesized Au NT-M-mSiO_2

The Au NTs were synthesized according to a previous report with modifications [54]. In Fig. S1, scanning transmission electron microscopy (STEM) images show the triangular platelet-like shape of the Au NTs where the edge length is about 67 nm and the thickness is about 22 nm. The vast majority of the NTs was found in the same orientation after dropcasting, lying with their large (111) facet on the support membrane. All NTs are known to have a central (111) twin plane as a result of the synthesis, which can not be observed in this orientation. The thickness across the NTs was quite uniform as is apparent from the contrast in the STEM images (Fig. S1c), and in general free of stacking faults. The main localized surface plasmon resonance (LSPR) band of the Au NTs was at 657 nm (Fig. S1e). Using as-synthesized Au NTs as seeds, three other metals, Ag, Pd, and Pt, were grown onto the Au NTs creating bimetallic core-shell nanoplatelets. The core-shell NPLs and the mSiO_2 coating were prepared by slightly modified protocols as our previous reports [55,56].

In Fig. 1 a-c the TEM images show the morphologies of the Au–Ag-mSiO_2, Au–Pd-mSiO_2, and Au–Pt-mSiO_2 core-shell-shell NPs, wherein the well-defined triangular shape is apparent for each type of bimetallic core-shell particle. The Ag shells grew into a smooth shell onto the single crystalline fcc Au NTs, while the Pd and Pt shells developed a rougher spikey structure. In the scanning transmission electron microscopy – high angle annular dark field (STEM-HAADF) images of Fig. 1 d-f, the dominant type of contrast is *Z* (atomic number) contrast whereby heavier elements appear brighter than lighter elements. Fig. 1d clearly shows the brighter Au cores at the center, and the Ag shells are visible as a grey layer outside the triangular Au cores, as

the atomic number of Au is higher than that of Ag. Similarly, the Pd shells appear darker than the Au cores in the STEM images (Fig. 1e). The STEM-X-ray energy-dispersive spectrometry (STEM-EDS) maps show the Au NT-M (Ag, Pd, Pt) core-shell structures (Fig. 1d–f). It should be pointed out that the atomic elements of the mSiO_2 shells are not visible in the HAADF-STEM images, because a camera length of 98 mm was used for imaging, which reduced the effects of electron diffraction from the nanocrystals and allowed a better Z contrast [57,58]. Because of this setting the signals from Si and O were not detectable. The Si and O elements are also not shown in all EDS maps in this work. In the elementary composition that was quantified from the EDS spectra, the atomic fraction of Au was about 70 at.%, 70 at.%, and 85 at.% in the Au–Ag, Au–Pd, and Au–Pt, NPTs respectively. Moreover, the plasmonic properties of the Au NT-M NPs were investigated by measuring the extinction spectra of the as-synthesized BMNPs with a UV–Vis spectrometer. As shown in Fig. S2, the main localized surface plasmon resonance (LSPR) band of both the Au NT-Ag ($\lambda_{LSPR} = 570$ nm) and Au NT-Pd NPs ($\lambda_{LSPR} = 650$ nm) showed a blue-shift compared to the LSPR of the Au NTs ($\lambda_{LSPR} = 657$ nm), while the main LSPR peak of the Au NT-Pt was at ~665 nm.

3.2. From core-shell to alloyed Au-M NPLs

To obtain fully alloyed bimetallic NPLs, we performed in-situ heating experiments on the silica-coated Au NT-M (Ag, Pd, Pt) core-shell NPLs. The experimental details are presented in the Supporting Information. The heating chips used had SiN_x windows thin enough that they were almost electron transparent and are visible as the bright areas in the TEM image shown in Fig. S3 and were used for all in-situ heating experiments. The heating curve and the corresponding STEM image at each temperature to which the Au–Ag NPLs were heated, are shown in Fig. S4 a and **b**, in which we found that the clear boundary of the Au core and Ag shell became more diffuse at 350 °C, and the two different grey values in one particle disappeared after heating for about 10 min at 400 °C, which means that at this temperature, the core-shell NPLs turned into alloyed particles while maintaining their triangular shape (Fig. 2a). STEM-EDS elemental maps were recorded of the particles at the same position on the grid after heating, and cooling down to 20 °C, to further confirm the formation of alloyed Au–Ag NPLs (Fig. S4c). In addition, no differences were found for particles inside the electron beam illuminated areas prior to and during the heating process (Figs. S5 and S6a) and particles outside these areas, which indicates that effects of the electron beam on the alloying process was negligible [32]. The alloying temperature of the Au–Ag NPLs (T~400 °C) was slightly lower than previous reports on similar Au–Ag NTs (T~450 °C) [40] and Au–Ag NRs (T~450 °C) [40,59], which could be caused by a difference in the composition used for the experiments and/or the shape factor (in the case of a comparison with NRs). For the plate-like NPs, the interdiffusion between two different atoms mainly occurs in (111) facets, while that of NRs is (100). The influence of composition on the alloying temperature

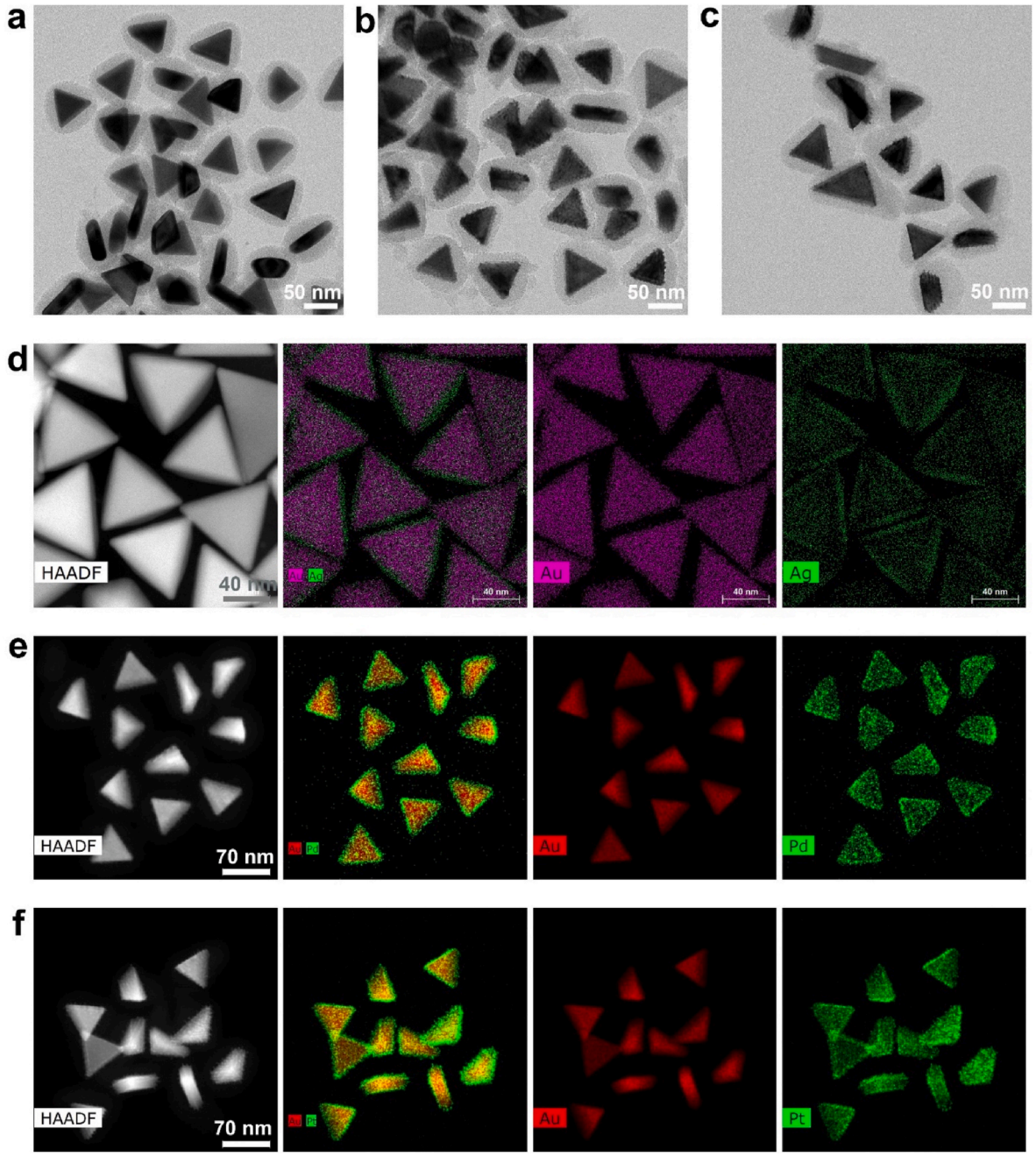

Fig. 1. Morphology and structure of Au NT-M (Ag, Pd, Pt)-mSiO$_2$ nanoparticles after synthesis. TEM image of a) Au NT-Ag-mSiO$_2$, b) Au NT-Pd-mSiO$_2$, c) Au NT-Pt-mSiO$_2$. STEM-EDS elemental maps of d) Au NT-Ag-mSiO$_2$, e) Au NT-Pd-mSiO$_2$, and f) Au NT-Pt-mSiO$_2$. The scale bar indicates 50 nm in a)-c), 40 nm in d), and 70 nm in e) and f).

of Au NRs has been well demonstrated by van der Hoeven et al. [60], which showed that a higher Ag content required a higher alloying temperature in the case of Au–Ag NRs.

Alloyed Au–Pd NPLs, having 70 at.% Au and 30 at.% Pd, were synthesized using the same strategy, but required a higher alloying temperature, as expected. The temperature-time curve of the in-situ heating is shown in Fig. S7a, and the relevant morphological evolutions of the Au–Pd NPLs from core-shell to alloyed configurations were recorded by STEM imaging (Fig. S7b and Fig. S8 a-g). The more rough, spikey Pd shells were found to change into smooth Pd layers covering the Au NT cores at 500 °C (Fig. 2b). The ability to achieve smooth core-shell morphologies may be important for a more homogeneous optimized catalytic performance as some of us recently showed for Au–Pd NR systems in the catalysis of hydrogenation reactions [61]. Next, the particles transformed into fully alloyed Au–Pd NPLs, with a preserved well-defined triangular shape, at 600 °C. Furthermore, the STEM-EDS maps both of particles lying on the monitored window and lying on a window not previously illuminated by the electron beam, confirmed the formation of Au–Pd NPLs (Fig. S7c and Fig. S9a) with still a triangular shape. The atomic ratio of Au and Pd was found to be the same before and after heating (Fig. S9b) from quantitative analysis of the EDS spectra from the chemical maps.

Au–Pt core-shell NPLs with 87 at.% Au and 13 at.% Pt content were used for the experiments, and fully alloyed Au–Pt particles were achieved at 650 °C (Fig. 2c, Fig. S10). The evolution was similar to that of the Au–Pd system; first, the rough, spikey Pt shell became smooth as the temperature was raised to 500 °C, following by the interdiffusion between the Au core and the Pt shell yielding a diffuse interface, while

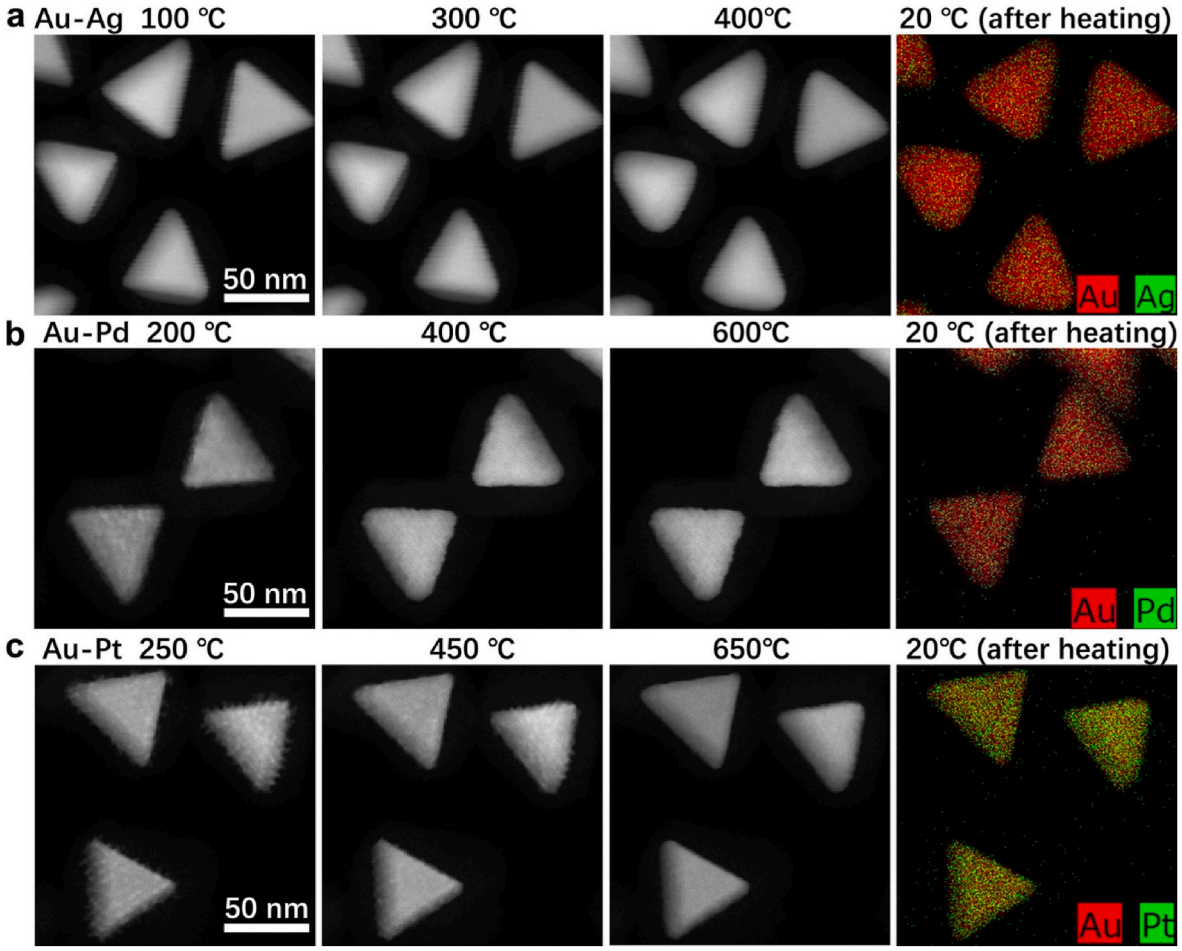

Fig. 2. Alloying of Au NT-M (Ag, Pd, Pt) NPLs. STEM images of (a) Au NT-Ag NPLs, (b) Au NT-Pd NPLs, and (c) Au NT-Pd NPLs, acquired at the different temperatures, and STEM-EDS elemental maps of alloyed Au-M (Ag, Pd, Pt) NTs acquired at 20 °C after heating.

complete alloying was observed after keeping the temperature at 650 °C for ~10 min, both in the time-evolution monitored windows (Fig. S11) and in not previously inspected windows (Fig. S12a). Quantification of EDS spectra showed that also here, the composition of the Au–Pt NPLs with triangular shape was almost the same as that of their core-shell predecessors (Fig. S12b). We also found that the alloying temperature of the Au–Pt core-shell NPLs was related to the content of the Pt component. As shown in Fig. S13, the Au–Pt NPLs were heated by using the same procedure for Au–Pd to 600 °C (Fig. S13a). For particles with a higher density of rough, spikey Pt crystals on the Au NT surface, marked as P1, P2, and P3 in Fig. S13 b and **c**, only partial alloying was found while other particles had already transformed to fully alloyed NPLs. The same trend was found for these particles on a different, not previously inspected SiNx windows (Figs. S14 and S15). Notably, the mesopores in $mSiO_2$ shell were remaining after heating at 600 °C (Fig. S16), which was in a good agreement with previous reports [62,63].

The alloying process of metals in nanomaterials strongly depends on the particle size, morphology, the chemical components, the temperature, and the heating time [40,60,64]. The above difference in alloying temperatures of Au-M core-shell NPLs for different shell metals is summarized in Scheme 1 and is mainly caused by their melting points which are listed in Table S1 (Appendix B). The bulk melting point of these four metals from low to high is in the order of Ag (962 °C), Au (1064 °C), Pd (1555 °C), and Pt (1769 °C) [5]. This explains why the alloying temperature of the Au–Ag system is lower than that of Au–Pd system, as both of them contain 70 at.% of Au and 30 at.% of Ag or Pd, that and the alloying temperature of Au–Pt NPLs, although they have 87 at.% Au and 13 at.% Pt content, is still higher than that of the other two bimetallic

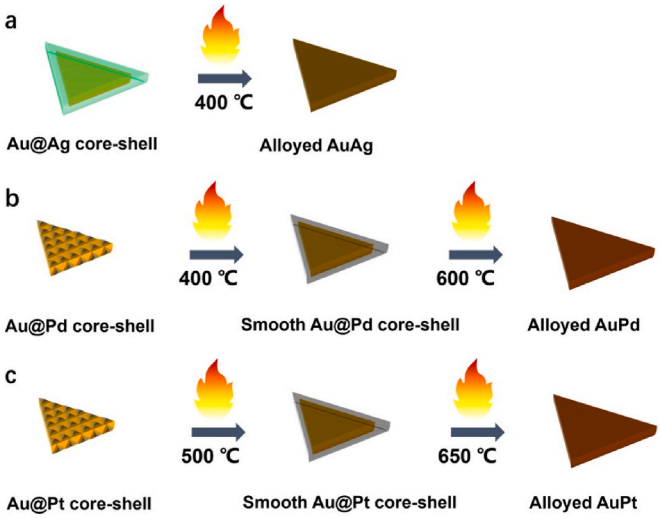

Scheme 1. Schematically illustration of the alloying process of Au-M (Ag, Pd, Pt) NPLs (Note: $mSiO_2$ shell is not showed in the scheme).

particles. On the other hand, the bond dissociation energy of the same metal (M-M) also plays a role. The bond dissociation energy of Pt (E_{Pt-Pt}) is 307 kJ/mol which is much higher than that of the other three metals (Table S1) [5]. Since in the oven the heating rate was slower and the

heating times were longer in comparison to the in-situ heating experiments, the alloyed Au-M were obtained at a lower temperature than in the ex-situ oven experiments. However, the alloying temperatures were still several hundreds of degrees below these bulk melting temperatures, which allowed the mesoporous silica shell to keep the out-of-equilibrium highly anisotropic particles shape to be retained while the particles nevertheless got fully alloyed with a drastic change in plasmonic and chemical properties.

3.3. From core-shell to alloyed and to Janus structure

To gain more insight into the high temperature-dependent phase behavior of the Au-M NPLs systems and their morphological stability, a set of in-situ heating experiments with fewer steps but reaching 1100 °C in 50 min, were conducted as well. In Fig. S17a, the temperature profile is shown that was applied to the $mSiO_2$ coated Au–Ag core-shell NPLs with 70 at.% of Au and 30 at.% of Ag. The corresponding STEM images and STEM-EDS maps show the formation of alloyed Au–Ag nanoparticles (Fig. S17 b, c). Most of the particles lost the well-defined triangular shape and became rounded, still having a strongly anisotropic shape though, while even some sharp triangular shapes were still present at temperatures as high as 900 °C. This deformation followed the same diffusion mechanism that we demonstrated in the case of Au NTs in our previous report [65]. In brief, it is driven by the minimization of the

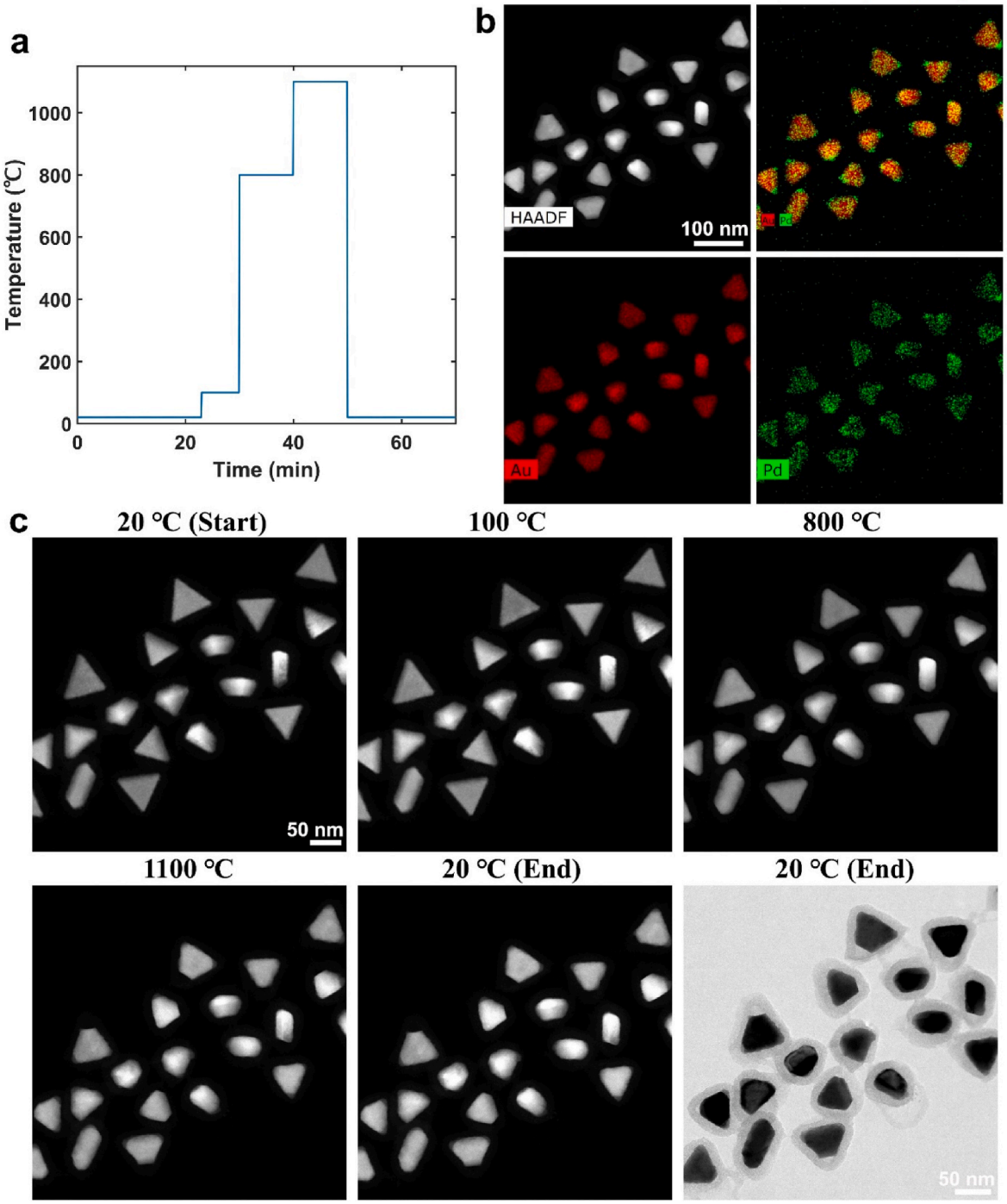

Fig. 3. Phase separation of Au–Pd NPLs. a) The temperature profile, b) STEM images of Au–Pd NPLs acquired at the different temperatures, and c) STEM-EDS elemental maps of alloyed Au–Pd NTs.

surface energy of the nanoparticles and the particles deformed by atomic diffusion that started from the corners and edges where the atoms have lower coordination numbers than at other positions and the curvature of the crystal shape is highest.

To further elucidate how high temperatures influenced the phase behavior and the morphology of the Au–Pd and Au–Pt NPs, similar heating experiments were applied to these NPLs as well. As shown in Fig. 3a and **b**, the STEM images acquired at each temperature step show that the Au–Pd core-shell NPLs changed into alloyed particles as the temperature was increased to 800 °C, while phase separation became apparent in the alloyed Au–Pd NPLs at 1100 °C. After keeping the sample at this temperature for 10 min and subsequent cooling down to 20 °C, the triangular shape of most of the particles had deformed into a trapezoidal shape, although for the Pt particles some sharp tipped triangles were still as well. The Pd in all the particles was found to have accumulated on the corners of the NPLs (Fig. 3b). The dynamic process of the phase separation was monitored by a STEM video recorded at 1100 °C and is added as supporting Movie S1. Due to the *Z* contrast, the Au and Pd atoms are easy to distinguish in the movie, wherein Au atoms diffused from the corners to the center of the particle and Pd atoms moved to the corners in a few minutes. Similar phase separation also took place in particles not previously exposed to the electron beam (Fig. S18 a, b). After the entire heating process, the SiO_2 shells still remained, covering all particles (Fig. S18 c, d) although almost certainly without the mesopores [63,66].

Fig. 4a shows the heating procedure applied to the Au–Pt core-shell NPLs. The STEM images acquired at each temperature reveal that similarly as with the Au–Pd particles, the structure of the NPLs changed from core-shell to alloyed, and finally turned into Janus-like structures (Fig. 4c), however with more triangular particles still being present even after the phase separation. Differently from the evolution in the Au–Pd system, the triangular shapes in most of the Au–Pt NPLs were well

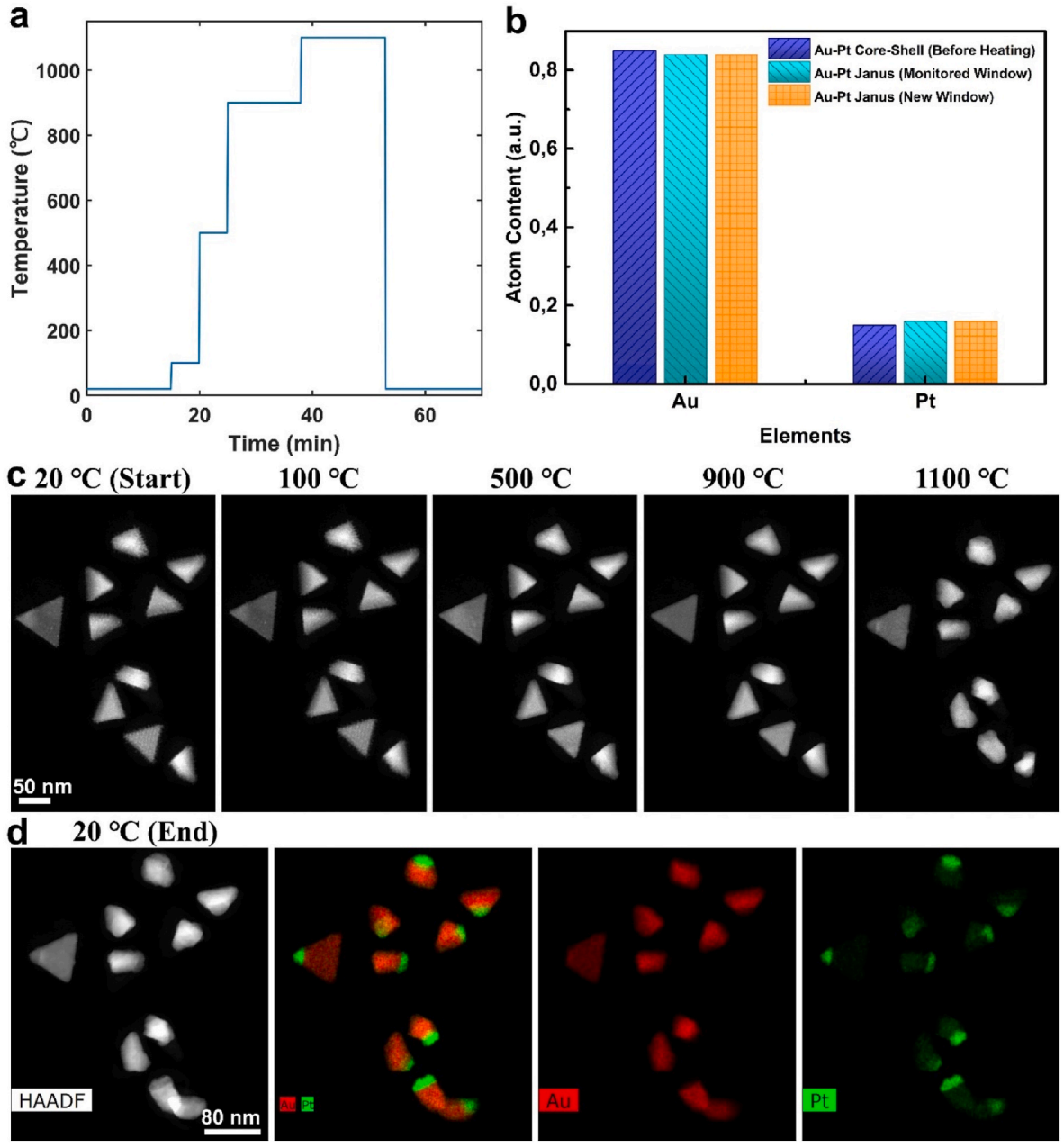

Fig. 4. Phase separation observed in Au–Pt NPLs. a) Temperature profile b) Elemental Au and Pt content in the NPLs before and after heating, c) STEM images of Au–Pt NPLs acquired at the different temperatures, and d) STEM-EDS elemental maps of Au–Pt Janus NPLs.

maintained, and in the Janus-like particles the Pt atoms were found to be mostly concentrated at one corner of the triangle (Fig. 4d). A movie recorded at 900 °C (Supporting Movie S2) demonstrates that Au and Pt content alloyed. As the temperature was raised to 1100 °C, two different grey values can be identified in one particle in the STEM recordings (Supporting Movie S3), which indicates the phase separation into Au and Pt. After about ~12 min of thermal treatment at 1100 °C, most of the Pt atoms moved to one corner and the remaining trapezoidal part of the triangle consisted of Au. Janus Au–Pt NPLs were also found formed different SiNx windows that had not been previously illuminated by the electron beam (Fig. S19).

For understanding of above alloying and phase separation behavior in bimetallic Au-M NPLs (summarized and showed in Scheme 2), the role of thermodynamics is important next to kinetic factors because the shape of all the particles even at the highest temperatures is far out of equilibrium, almost certainly kept in this state due to the silica layer. It may be that the much higher retentions of shape of the NTs in this study at temperatures as high as 1100 °C are caused by the fact that the mesopores at some points were annealed out causing the silica layer to most likely become denser and stronger, even although the higher temperatures are also close to the melting point of silica. That the mixing entropy at elevated temperatures could overcome the much larger dissimilarities between the Au and Pd and Pt atoms as compared to the Ag and Au atoms which are much more similar in size and interaction strength can be understood. It is less easy to understand that the free energy at even higher temperatures would result in the phase separation observed. It needs to remain for future work to better understand this behavior and see in how far this is also influenced by the silica layer.

For the Au–Ag system, our experiments show that the alloying is preferred and that phase segregation did not take place as at the elevated temperatures as observed for the Au–Pd and Au–Pt NPLs. This is in good agreement with previously calculated Au–Ag phase diagrams of nanospheres [67], in which the stable alloyed Au–Ag area is large, and a Janus structure does not exist [42]. As already mentioned, the average surface energies of Au and Ag (shown in Appendix B Table S1), the interface energy per unit area between Au and Ag ($\sigma = -0.149\ J/m^2$) [67] is quite small, thus the difference in interface energy between core-shell and Janus in Au–Ag NPLs is also small. In this case, as the average surface energy of Au (1.50 J/m^2) is larger than that of Ag (1.24 J/m^2) [68], the free energy of the Au–Ag Janus structure is less favorable than that of a core-shell structure, and therefore, the alloyed NPLs do not phase separate as at higher temperatures the mixing entropy only becomes more important. Second, the high miscibility of Au and Ag is high, as both have the same fcc crystal structure with a negligible difference of lattice parameters and atomic radius (Table S1) [5]. In addition, the formation enthalpy of the chemical bond between Au and Ag ($E_{Au\text{-}Ag}$) is negative (The bond dissociation energies of Au–Au, Au–Ag, and Ag–Ag are shown in Table S1) [5]. The bulk phase diagram of Au and Ag predicts a continuous Au–Ag solid solution over the entire compositional range. Due to these reasons, alloying will spontaneously take place in Au–Ag NPLs when sufficient heating is applied.

The morphological evolution of the Au–Pd and Au–Pt NPLs systems were found to be similar, and we will take the Au–Pt system as representative for the discussion of both systems. Although Au and Pt share the same fcc-type crystal structure, their lattice parameters and atomic radius are quite different (shown in Table S1) [5]. As predicted in the Au–Pt in phase diagram [52,69] and previous molecular dynamics simulation studies on spherical Au–Pt nanoparticles with sizes up to ~20 nm, the Au–Pt system is only partly miscible and the thermodynamic stability of Au–Pt bimetallic structures is Pt (core)-Au (shell) > Janus > alloy > Au (core)-Pt (shell) [48,51]. There are several reasons for this order. First, the surface energy of Au (1.50 J/m^2) is much lower than that of Pt (2.49 J/m^2) [70]. Hence, a Pt (core)-Au (shell) structure is more stable than the inverse structure and a Janus structure. Second, the strain energy caused by the lattice mismatch of Au and Pt make an alloyed particles less stable than the Pt (core)-Au (shell) and Janus structures [48,51]. Apparently, for the composition studied in this work the configurational entropy of alloying is at some temperature enough to favor the formation of an alloyed structure.

Another interesting finding is the shape stability of the $mSiO_2$ coated Au–Pt system, which is much higher than that of pure Au and Au–Ag, and Au–Pd NPLs. First, all Au-M NPLs were stabilized by the $mSiO_2$ coating, which helps in retaining the morphology of the nanoparticles as has been well illustrated in many studies of nanoparticles of various shapes, e.g. Au nanorods (NRs) [31,33], Au-M NRs [32], Au NTs [65], Au–Ag NTs [40], and Pt nanoparticles [63]. Furthermore, it is well known that the melting point of nanoparticles strongly depend on their size [71]; with the growth of additional metals (Ag, Pd, Pt) onto the Au NTs, the volume of the particles as a whole becomes larger, which results in Au NT-M (Ag, Pd, Pt) NPLs being more stable than pure Au NTs. The shape of the Au–Pt NPLs discussed above were found to be more stable than in the case of the Au–Ag and Au–Pd systems, although the atomic fraction of Pt was only ~13 at.%, while the atomic fractions of Ag and Pd were ~30 at.%, which means that more Ag and Pd were grown onto the same Au NTs. This is plausibly explained by the considerably higher melting point of Pt in comparison to that of the other three metals (Table S1) [5]. Previous investigation has shown the same trend in the alloying of Au-M (Ag, Pd, Pt) NRs, [59]. Considering that the shape stability of nanoparticles is crucial for the optical and catalytic properties, this is of major importance to the applicability to catalytic reactions taking place at high temperatures.

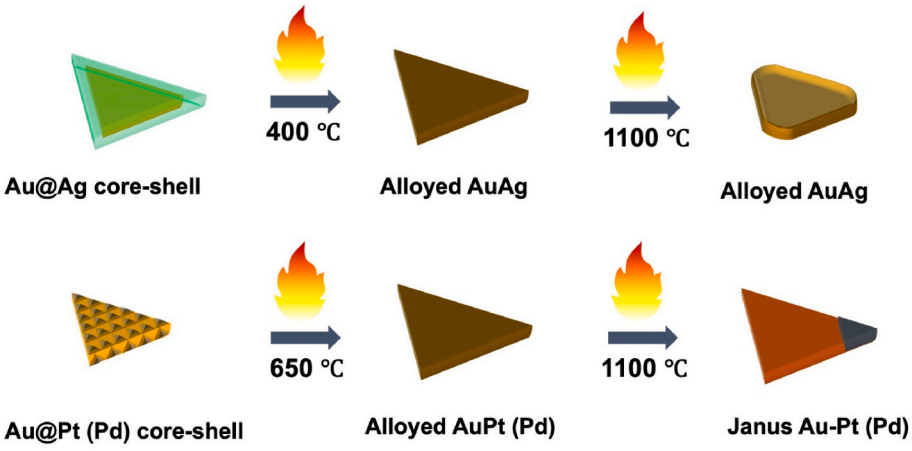

Scheme 2. Schematically illustration of the alloying and phase segregating process of Au-M (Ag, Pd, Pt) NPLs (Note: $mSiO_2$ shell is not showed in the scheme).

4. Conclusion

In summary, fully alloyed Au-M (Ag, Pd, and Pt) NPLs with well-defined triangular plate-like shapes were prepared successfully by heating the $mSiO_2$ coated, initially core-shell NPLs to a temperature which was at least 300 °C below the melting temperatures of the metals involved. The alloying temperatures of the core-shell NPLs were much lower than those in bulk metals due to nanoscale size effects, and mainly depend on the melting point and mole fraction of the shell metals when keeping the core metal. Moreover, the rough, spikey Pd and Pt shells as grown at room temperature could be turned into smooth shells covering the Au NT cores when the particles were heated to 500 °C, which is similar to the Au–Ag morphology and allows for a better controlled morphology comparison for these bi-metallic systems. Interestingly, phase separation was found to take place for the Au–Pd and Au–Pt systems at 1100 °C, leading to the formation of Au–Pt Janus NPLs. The dynamic process as monitored by in-situ STEM imaging show that the overall evolution took place starting with a core-shell morphology changing to an alloyed configuration and subsequently changing to Janus-like particles. Furthermore, the thermal stability of the bimetallic Au-M core-shell NPLs was found to be significantly enhanced in comparison to the monometallic Au NTs, due to the coating with the second metal, as the volume increases after overgrowth which results in a higher melting temperature and a more stable shape. These findings and insights are of importance to further investigations of well-defined bimetallic and multimetallic nano-systems with well-defined different morphologies ranging from core-shell to fully alloyed and Janus-type all an anisotropic triangular shape will allow for optimization of plasmonic and chemical properties of these particles for applications in catalysis, sensing, biomedicine, and energy conversion.

CRediT authorship contribution statement

Xiaobin Xie: Writing – review & editing, Writing – original draft, Visualization, Validation, Investigation, Conceptualization. **Alfons van Blaaderen:** Writing – review & editing, Supervision, Resources, Project administration, Funding acquisition. **Marijn A. van Huis:** Writing – review & editing, Supervision, Resources, Methodology, Investigation, Funding acquisition, Formal analysis.

Declaration of competing interest

The authors declare that they have no known competing financial interests or personal relationships that could have appeared to influence the work reported in this paper.

Data availability

Data will be made available on request.

Acknowledgements

We thank Dr. Da Wang and Dr. Jessi van der Hoeven for the fruitful discussions. X. X., M. A. v. H. and A. v. B. acknowledge financial support from EU H2020-MSCA-ITN-2015 project 'MULTIMAT' (project number: 676045). M. A. v. H. acknowledges the European Research Council for an ERC-Consolidator grant (NANO-INSITU, grant no. 683076).

Appendix B. Supplementary data

Supplementary data to this article can be found online at https://doi.org/10.1016/j.mtnano.2024.100462.

References

[1] C. Chen, et al., Highly crystalline multimetallic nanoframes with three-dimensional electrocatalytic surfaces, Science 343 (2014) 1339–1343, https://doi.org/10.1126/science.1249061.
[2] Z. Fan, H. Zhang, Template synthesis of noble metal nanocrystals with unusual crystal structures and their catalytic applications, Acc. Chem. Res. 49 (2016) 2841–2850, https://doi.org/10.1021/acs.accounts.6b00527.
[3] Y. Qu, R. Cheng, Q. Su, X. Duan, Plasmonic enhancements of photocatalytic activity of Pt/n-Si/Ag photodiodes using Au/Ag core/shell nanorods, J. Am. Chem. Soc. 133 (2011) 16730–16733, https://doi.org/10.1021/ja204383q.
[4] H. Jing, et al., Tunable plasmonic nanoparticles with catalytically active high-index facets, Nano Lett. 14 (2014) 3674–3682, https://doi.org/10.1021/nl5015734.
[5] K.D. Gilroy, A. Ruditskiy, H.C. Peng, D. Qin, Y. Xia, Bimetallic nanocrystals: syntheses, properties, and applications, Chem. Rev. 116 (2016) 10414–10472, https://doi.org/10.1021/acs.chemrev.6b00211.
[6] X. Huang, et al., Plasmonic and catalytic AuPd nanowheels for the efficient conversion of light into chemical energy, Angew Chem. Int. Ed. Engl. 52 (2013) 6063–6067, https://doi.org/10.1002/anie.201301096.
[7] E.M. Larsson, C. Langhammer, I. Zoric, B. Kasemo, Nanoplasmonic probes of catalytic reactions, Science 326 (2009) 1091–1094, https://doi.org/10.1126/science.1176593.
[8] N. Becknell, et al., Control of architecture in rhombic dodecahedral Pt-Ni nanoframe electrocatalysts, J. Am. Chem. Soc. 139 (2017) 11678–11681, https://doi.org/10.1021/jacs.7b05584.
[9] X. Zhu, et al., Realization of red plasmon shifts up to approximately 900 nm by AgPd-tipping elongated Au nanocrystals, J. Am. Chem. Soc. 139 (2017) 13837–13846, https://doi.org/10.1021/jacs.7b07462.
[10] M. Chen, et al., Core-shell Pd@Au nanoplates as theranostic agents for in-vivo photoacoustic imaging, CT imaging, and photothermal therapy, Adv. Mater. 26 (2014) 8210–8216, https://doi.org/10.1002/adma.201404013.
[11] S. Zaleski, et al., Investigating nanoscale electrochemistry with surface- and tip-enhanced Raman spectroscopy, Acc. Chem. Res. 49 (2016) 2023–2030, https://doi.org/10.1021/acs.accounts.6b00327.
[12] S.S. Sinha, S. Jones, A. Pramanik, P.C. Ray, Nanoarchitecture based SERS for biomolecular fingerprinting and label-free disease markers diagnosis, Acc. Chem. Res. 49 (2016) 2725–2735, https://doi.org/10.1021/acs.accounts.6b00384.
[13] X. Xie, et al., Toward hybrid Au nanorods @ M (Au, Ag, Pd and Pt) core-shell heterostructures for ultrasensitive SERS probes, Nanotechnology 28 (2017) 245602, https://doi.org/10.1088/1361-6528/aa70f3.
[14] Z. Lou, M. Fujitsuka, T. Majima, Pt-Au triangular nanoprisms with strong dipole plasmon resonance for hydrogen generation studied by single-particle spectroscopy, ACS Nano 10 (2016) 6299–6305, https://doi.org/10.1021/acsnano.6b02494.
[15] H. Huang, et al., Unraveling surface plasmon decay in core-shell nanostructures toward broadband light-driven catalytic organic synthesis, J. Am. Chem. Soc. 138 (2016) 6822–6828, https://doi.org/10.1021/jacs.6b02532.
[16] Y. Wang, et al., Ensemble effect in bimetallic electrocatalysts for CO2 reduction, J. Am. Chem. Soc. 141 (2019) 16635–16642, https://doi.org/10.1021/jacs.9b05766.
[17] J.E. Millstone, et al., Observation of a quadrupole plasmon mode for a colloidal solution of gold nanoprisms, J. Am. Chem. Soc. 127 (2005) 5312–5313, https://doi.org/10.1021/ja043245a.
[18] M.N. O'Brien, M.R. Jones, K.L. Kohlstedt, G.C. Schatz, C.A. Mirkin, Uniform circular disks with synthetically tailorable diameters: two-dimensional nanoparticles for plasmonics, Nano Lett. 15 (2015) 1012–1017, https://doi.org/10.1021/nl5038566.
[19] Y. Zhai, et al., Polyvinylpyrrolidone-induced anisotropic growth of gold nanoprisms in plasmon-driven synthesis, Nat. Mater. 15 (2016) 889–895, https://doi.org/10.1038/nmat4683.
[20] M.B. Cortie, A.M. McDonagh, Synthesis and optical properties of hybrid and alloy plasmonic nanoparticles, Chem. Rev. 111 (2011) 3713–3735, https://doi.org/10.1021/cr1002529.
[21] H. Liu, et al., Etching-free epitaxial growth of gold on silver nanostructures for high chemical stability and plasmonic activity, Adv. Funct. Mater. 25 (2015) 5435–5443, https://doi.org/10.1002/adfm.201502366.
[22] S.-Y. Ding, et al., Nanostructure-based plasmon-enhanced Raman spectroscopy for surface analysis of materials, Nat. Rev. Mater. 1 (2016) 16021, https://doi.org/10.1038/natrevmats.2016.21.
[23] Y. Kong, G. Zhang, C. Wang, Y. Ma, Y. Zheng, Seed surface doping-mediated seeded growth of Au–Ag Janus nanoparticles with tunable sizes and multiple plasmonic absorption modes, CrystEngComm 24 (2022) 6392–6399, https://doi.org/10.1039/d2ce00962e.
[24] Y. Zheng, et al., Seeded growth of gold-copper Janus nanostructures as a tandem catalyst for efficient electroreduction of CO(2) to C(2+) products, Small 18 (2022) e2201695, https://doi.org/10.1002/smll.202201695.
[25] D. Knez, et al., The impact of swift electrons on the segregation of Ni-Au nanoalloys, Appl. Phys. Lett. 115 (2019), https://doi.org/10.1063/1.5093472.
[26] P. Thaler, et al., Formation of bimetallic core-shell nanowires along vortices in superfluid He nanodroplets, Phys. Rev. B 90 (2014), https://doi.org/10.1103/PhysRevB.90.155442.
[27] D. Knez, et al., Modelling electron beam induced dynamics in metallic nanoclusters, Ultramicroscopy 192 (2018) 69–79, https://doi.org/10.1016/j.ultramic.2018.05.007.
[28] L. Huang, et al., Shape regulation of high-index facet nanoparticles by dealloying, Science 365 (2019) 1159–1163, https://doi.org/10.1126/science.aax5843.

[29] H. Mistry, A.S. Varela, S. Kühl, P. Strasser, B.R. Cuenya, Nanostructured electrocatalysts with tunable activity and selectivity, Nat. Rev. Mater. 1 (2016) 16009, https://doi.org/10.1038/natrevmats.2016.9.
[30] C. Hanske, M.N. Sanz-Ortiz, L.M. Liz-Marzan, Silica-coated plasmonic metal nanoparticles in action, Adv. Mater. 30 (2018) e1707003, https://doi.org/10.1002/adma.201707003.
[31] W. Albrecht, et al., Single particle deformation and analysis of silica-coated gold nanorods before and after femtosecond laser pulse excitation, Nano Lett. 16 (2016) 1818–1825, https://doi.org/10.1021/acs.nanolett.5b04851.
[32] Y. Bai, C. Gao, Y. Yin, Fully alloyed Ag/Au nanorods with tunable surface plasmon resonance and high chemical stability, Nanoscale 9 (2017) 14875–14880, https://doi.org/10.1039/c7nr06002e.
[33] W. Albrecht, et al., Impact of the electron beam on the thermal stability of gold nanorods studied by environmental transmission electron microscopy, Ultramicroscopy (2018), https://doi.org/10.1016/j.ultramic.2018.05.006.
[34] X. Huang, T. Jones, H. Fan, M.-G. Willinger, Atomic-scale observation of irradiation-induced surface oxidation by in situ transmission electron microscopy, Adv. Mater. Interfac. 3 (2016) 1600751, https://doi.org/10.1002/admi.201600751.
[35] Y. He, et al., In situ observation of shear-driven amorphization in silicon crystals, Nat. Nanotechnol. 11 (2016) 866–871, https://doi.org/10.1038/nnano.2016.166.
[36] T. Eggebrecht, et al., Light-Induced metastable magnetic texture uncovered by in situ lorentz microscopy, Phys. Rev. Lett. 118 (2017) 097203, https://doi.org/10.1103/PhysRevLett.118.097203.
[37] X. Fu, B. Chen, J. Tang, M.T. Hassan, A.H. Zewail, Imaging rotational dynamics of nanoparticles in liquid by 4D electron microscopy, Science 355 (2017) 494–498, https://doi.org/10.1126/science.aah3582.
[38] S.F. Tan, G. Lin, M. Bosman, U. Mirsaidov, C.A. Nijhuis, Real-time dynamics of galvanic replacement reactions of silver nanocubes and Au studied by liquid-cell transmission electron microscopy, ACS Nano 10 (2016) 7689–7695, https://doi.org/10.1021/acsnano.6b03020.
[39] X. Ye, et al., Single-particle mapping of nonequilibrium nanocrystal transformations, Science 354 (2016) 874–877, https://doi.org/10.1126/science.aah4434.
[40] A. Skorikov, et al., Quantitative 3D characterization of elemental diffusion dynamics in individual Ag@Au nanoparticles with different shapes, ACS Nano 13 (2019) 13421–13429, https://doi.org/10.1021/acsnano.9b06848.
[41] D. Jana, A. Dandapat, G. De, Au@Pd Core−Shell nanoparticle incorporated alumina sols and coatings transformation of Au@Pd to Au−Pd alloy nanoparticles, J. Phys. Chem. C 113 (2009) 9101–9107.
[42] G. Guisbiers, et al., Electrum, the gold-silver alloy, from the bulk scale to the nanoscale: synthesis, properties, and segregation rules, ACS Nano 10 (2016) 188–198, https://doi.org/10.1021/acsnano.5b05755.
[43] S. Zhou, G.S. Jackson, B. Eichhorn, AuPt alloy nanoparticles for CO-tolerant hydrogen activation architectural effects in Au-Pt bimetallic nanocatalysts, Adv. Funct. Mater. 17 (2007) 3099–3104.
[44] B.N. Wanjala, et al., Nanoscale alloying, phase-segregation, and Core−Shell evolution of Gold−Platinum nanoparticles and their electrocatalytic effect on oxygen reduction reaction, Chem. Mater. 22 (2010) 4282–4294, https://doi.org/10.1021/cm101109e.
[45] D. Bochicchio, R. Ferrando, Morphological instability of core-shell metallic nanoparticles, Phys. Rev. B 87 (2013), https://doi.org/10.1103/PhysRevB.87.165435.
[46] F. Calvo, Thermodynamics of nanoalloys, Phys. Chem. Chem. Phys. 17 (2015) 27922–27939, https://doi.org/10.1039/c5cp00274e.
[47] M. Cui, H. Lu, H. Jiang, Z. Cao, X. Meng, Phase diagram of continuous binary nanoalloys: size, shape, and segregation effects, Sci. Rep. 7 (2017) 41990, https://doi.org/10.1038/srep41990.
[48] V. Petkov, et al., Pt-Au alloying at the nanoscale, Nano Lett. 12 (2012) 4289–4299, https://doi.org/10.1021/nl302329n.
[49] L. Deng, W. Hu, H. Deng, S. Xiao, Surface segregation and structural features of bimetallic Au−Pt nanoparticles, J. Phys. Chem. C 114 (2010) 11026–11032.
[50] A.J. Logsdail, R.L. Johnston, Predicting the optical properties of core–shell and Janus segregated Au–M nanoparticles (M = Ag, Pd), J. Phys. Chem. C 116 (2012) 23616–23628, https://doi.org/10.1021/jp306000u.
[51] Y. Wang, M. Hou, Ordering of bimetallic nanoalloys predicted from bulk alloy phase diagrams, J. Phys. Chem. C 116 (2012) 10814–10818, https://doi.org/10.1021/jp302260b.
[52] J.J. Burton, E.S. Machlin, Prediction of segregation to alloy surfaces from bulk phase diagrams, Phys. Rev. Lett. 37 (1976) 1433–1436, https://doi.org/10.1103/PhysRevLett.37.1433.
[53] N. Eom, M.E. Messing, J. Johansson, K. Deppert, General trends in core-shell preferences for bimetallic nanoparticles, ACS Nano 15 (2021) 8883–8895, https://doi.org/10.1021/acsnano.1c01500.
[54] L. Scarabelli, M. Coronado-Puchau, J.J. Giner-Casares, J. Langer, L.M. Liz-Marzań, Monodisperse gold nanotriangles size control, large-scale self-assembly, and performance in surface-enhanced Raman scattering, ACS Nano 8 (2014) 5833–5842.
[55] X. Xie, M.A. van Huis, A. van Blaaderen, Symmetric and asymmetric epitaxial growth of metals (Ag, Pd, and Pt) onto Au nanotriangles: effects of reductants and plasmonic properties, Nanoscale 13 (2021) 2902–2913, https://doi.org/10.1039/d0nr06789j.
[56] X. Xie, M.A. van Huis, A. van Blaaderen, Single-step coating of mesoporous SiO(2) onto nanoparticles: growth of yolk-shell structures from core-shell structures, Nanoscale 13 (2021) 10925–10932, https://doi.org/10.1039/d1nr01242h.
[57] S. Yamashita, et al., Atomic number dependence of Z contrast in scanning transmission electron microscopy, Sci. Rep. 8 (2018) 12325, https://doi.org/10.1038/s41598-018-30941-5.
[58] S.J. Pennycook, Z-contrast stem for materials science, Ultramicroscopy 30 (1989) 58–69, https://doi.org/10.1016/0304-3991(89)90173-3.
[59] W. Albrecht, J.E. van der Hoeven, T.S. Deng, P.E. de Jongh, A. van Blaaderen, Fully alloyed metal nanorods with highly tunable properties, Nanoscale 9 (2017) 2845–2851, https://doi.org/10.1039/c6nr08484b.
[60] J.E.S. van der Hoeven, et al., In situ observation of atomic redistribution in alloying gold-silver nanorods, ACS Nano 12 (2018) 8467–8476, https://doi.org/10.1021/acsnano.8b03978.
[61] J.E.S. van der Hoeven, et al., Unlocking synergy in bimetallic catalysts by core-shell design, Nat. Mater. 20 (2021) 1216–1220, https://doi.org/10.1038/s41563-021-00996-3.
[62] Z. Teng, et al., Mesoporous organosilica hollow nanoparticles: synthesis and applications, Adv. Mater. 31 (2019) e1707612, https://doi.org/10.1002/adma.201707612.
[63] S.H. Joo, et al., Thermally stable Pt/mesoporous silica core-shell nanocatalysts for high-temperature reactions, Nat. Mater. 8 (2009) 126–131, https://doi.org/10.1038/nmat2329.
[64] T. Shibata, et al., Size-dependent spontaneous alloying of Au-Ag nanoparticles, J. Am. Chem. Soc. 124 (2002) 11989–11996, https://doi.org/10.1021/ja026764r.
[65] X. Xie, W. Albrecht, M.A. van Huis, A. van Blaaderen, Unexpectedly high thermal stability of Au Nanotriangle@mSiO2 yolk-shell nanoparticles, Nanoscale (2024), https://doi.org/10.1039/D3NR05916B.
[66] V. Zelenak, V. Hornebecq, S. Mornet, O. Schaf, P. Llewellyn, Mesoporous silica modified with titania structure and thermal stability, Chem. Mater. 18 (2006) 3184–3191.
[67] H. Peng, W. Qi, S. Li, W. Ji, Modeling the phase stability of Janus, core–shell, and alloyed Ag–Cu and Ag–Au nanoparticles, J. Phys. Chem. C 119 (2015) 2186–2195, https://doi.org/10.1021/jp510725a.
[68] C.L. Liu, J.M. Cohen, J.B. Adams, A.F. Voter, Eam study of surface self-diffusion of single adatoms of fcc metals Ni, Cu, Al, Ag, Au, Pd, and Pt, Surf. Sci. 253 (1991) 334–344, https://doi.org/10.1016/0039-6028(91)90604-Q.
[69] H. Okamoto, T.B. Massalski, The Au−Pt (Gold-Platinum) system, Bulletin of Alloy Phase Diagrams 6 (1985) 46–47.
[70] K. Yun, et al., Monte Carlo simulations of the structure of Pt-based bimetallic nanoparticles, Acta Mater. 60 (2012) 4908–4916, https://doi.org/10.1016/j.actamat.2012.05.032.
[71] K. Dick, T. Dhanasekaran, Z. Zhang, D. Meisel, Size-dependent melting of silica-encapsulated gold nanoparticles, J. Am. Chem. Soc. 124 (2002) 2312.